AFRL-AFOSR-VA-TR-2023-0022

High Reynolds Number Quiet Mach 6 Nozzle Fabrication and Natural Transition Experiments

Thomas Corke
UNIVERSITY OF NOTRE DAME DU LAC
940 GRACE HALL
NOTRE DAME, IN, 46556
USA

10/04/2022
Final Technical Report

Air Force Research Laboratory
Air Force Office of Scientific Research
Arlington, Virginia 22203
Air Force Materiel Command

REPORT DOCUMENTATION PAGE

PLEASE DO NOT RETURN YOUR FORM TO THE ABOVE ORGANIZATION.

1. REPORT DATE	2. REPORT TYPE	3. DATES COVERED	
20221004	Final	START DATE 20170901	END DATE 20210228

4. TITLE AND SUBTITLE
High Reynolds Number Quiet Mach 6 Nozzle Fabrication and Natural Transition Experiments

5a. CONTRACT NUMBER	5b. GRANT NUMBER	5c. PROGRAM ELEMENT NUMBER
	FA9550-17-1-0347	61102F
5d. PROJECT NUMBER	**5e. TASK NUMBER**	**5f. WORK UNIT NUMBER**

6. AUTHOR(S)
Thomas Corke

7. PERFORMING ORGANIZATION NAME(S) AND ADDRESS(ES)
UNIVERSITY OF NOTRE DAME DU LAC
940 GRACE HALL
NOTRE DAME, IN 46556
USA

8. PERFORMING ORGANIZATION REPORT NUMBER

9. SPONSORING/MONITORING AGENCY NAME(S) AND ADDRESS(ES)	10. SPONSOR/MONITOR'S ACRONYM(S)	11. SPONSOR/MONITOR'S REPORT NUMBER(S)
Air Force Office of Scientific Research 875 N. Randolph St. Room 3112 Arlington, VA 22203	AFRL/AFOSR RTA1	AFRL-AFOSR-VA-TR-2023-0022

12. DISTRIBUTION/AVAILABILITY STATEMENT
A Distribution Unlimited: PB Public Release

13. SUPPLEMENTARY NOTES

14. ABSTRACT
The program involves the fabrication of the expansion portion of the “quiet” nozzle of the Notre Dame Large Mach 6 Quiet Tunnel, as well as an experiment to be performed in the new tunnel that investigates the role of roughness on blunt cone frustum transition. The facility is designed to accommodate models greater than 2 m. in length that reside completely within the quiet region, and reach x-Reynolds numbers of 40M where flight tests indicate turbulent transition occurs. The test article was designed to exploit the large test section. It consists of a 1.6m long 7deg. half-angle right-circular cone. The cone is deigned with two nose tip sections that allow 7 different nose tips of different radii to be installed. The larger nose radii are designed to reach conditions that result in neutral growth of the 2nd mode instability, and ultimately transition length reversal. Continued delays in the operation of the Notre Dame quiet tunnel resulted in performing the experiments in the U.S. Air Force Academy Mach 6 Ludwieg tube. This utilized a repurposed 7deg. cone model whose length was extended to achieve natural transition on the model at higher unit Reynolds numbers. This model has three interchangeable nose tips of different radii, with the largest radius capable of neutral 2nd mode growth at the highest unit Reynolds number. The measurements consisted of off-wall measuRements of total pressure and total temperature using specially developed high-bandwidth pressure and temperature sensors. The preliminary results look promising, showing differences in the boundary layer development attributable to the nose radius Reynolds numbers.

15. SUBJECT TERMS

16. SECURITY CLASSIFICATION OF:			17. LIMITATION OF ABSTRACT	18. NUMBER OF PAGES
a. REPORT	b. ABSTRACT	c. THIS PAGE		
U	U	U	UU	24

19a. NAME OF RESPONSIBLE PERSON	19b. PHONE NUMBER *(Include area code)*
SARAH POPKIN	000-0000

To: technicalreports@afosr.af.mil

Subject: Final Progress Statement to Dr. Sarah Popkin

Contract/Grant Title: High Reynolds Number Quiet Mach 6 Nozzle Fabrication and Natural Transition Experiments

Principle Investigator: Thomas C. Corke (PI), Thomas J. Juliano (Co-PI), University of Notre Dame

Contract/Grant No.: FA9550-17-1-0347

Reporting Period: September 1, 2017 to February 28, 2021

Abstract

The program involves the fabrication of the expansion portion of the quiet nozzle of the Notre Dame Large Mach 6 Quiet Tunnel, as well as an experiment to be performed in the new tunnel that investigates the role of roughness on blunt cone frustum transition.The facility is designed to accommodate models greater than 2 m. in length that reside completely within the quiet region, and reach x-Reynolds numbers of 40M where flight tests indicate turbulent transition occurs. The test article was designed to exploit the large test section. It consists of a 1.6m long 7deg. half-angle right-circular cone. The cone is deigned with two nose tip sections that allow 7 different nose tips of different radii to be installed. The larger nose radii are designed to reach conditions that result in neutral growth of the 2nd mode instability, and ultimately transition length reversal. Continued delays in the operation of the Notre Dame quiet tunnel resulted in performing the experiments in the U.S. Air Force Academy Mach 6 Ludwieg tube. This utilized a repurposed 7deg. cone model whose length was extended to achieve natural transition on the model at higher unit Reynolds numbers. This model has three interchangeable nose tips of different radii, with the largest radius capable of neutral 2nd mode growth at the highest unit Reynolds number. The measurements consisted of off-wall measurements of total pressure and total temperature using specially developed high-bandwidth pressure and temperature sensors. The preliminary results look promising, showing differences in the boundary layer development attributable to the nose radius Reynolds numbers.

Summary Accomplishments:

Mach 6 Quiet Tunnel. The program involved the fabrication of the diverging portion of the "quiet" nozzle of the AFOSR-UND Large Mach 6 Quiet Tunnel, as well as an experiment to be performed in the new tunnel that investigates the role of roughness on blunt cone frustum transition. In a quiet hypersonic tunnel, the nozzle geometry is designed to maintain for as long as possible, laminar flow of the boundary layers on the nozzle side walls. This ultimately relies on suppressing the growth of boundary layer instabilities, most notably Tollmien-Schlichting, Mack 2^{nd} mode, and Taylor-Görtler. The latter is addressed by designing the nozzle with a slow area expansion in which the axial curvature maintains a sub-critical Taylor-Görtler number. In our large x-Reynolds number design, this results in a very long nozzle. Suppressing the Tollmien-Schlichting instability involves a combination of boundary layer suction at the nozzle throat, highly polished nozzle walls to minimizing surface roughness, and an additional feature in our design, nozzle wall heating. The facility is designed to accommodate models greater than 2 m in length that reside completely within the quiet region, and reach x-Reynolds numbers of 40×10^6 where flight tests indicate turbulent transition occurs. The building enclosing the wind tunnel is specially designed to meet facility clearance requirements.

The nozzle expansion was designed through a collaboration with Boeing and reported on by Lakebrink et al. [2016]. The design deviated from the earlier (1980) approach developed at NASA Langley[Beckwith et al., 1988] by performing a parametric design optimization that sought to minimize the overall nozzle expansion length while maintaining sufficiently low disturbance amplification factors and uniform flow at the exit plane. The resulting design reduced the nozzle length by 40%. This reduced the material and fabrication cost, with the savings being used to fabricate *two* identical geometry nozzle expansion sections; one of highly polished stainless-steel that will be the final nozzle expansion section, and the other a "surrogate" nozzle expansion section made of Aluminum. The surrogate nozzle expansion is completely identical to the stainless-steel expansion section. The surrogate nozzle expansion was installed first. This provided a check on the various components and assembly approach that could benefit the assembly of the stainless-steel expansion section. Although not polished to the same degree, the surrogate nozzle expansion is expected to result in quiet flow at lower stagnation pressures. Therefore it provides a means to initially document the tunnel operation and flow quality, including the critical first operation of the fast-acting valve located just upstream of the nozzle throat. The experience gained at this stage is intended to lessen the risk of damaging the final stainless-steel nozzle. To date, the surrogate nozzle is the only one installed in the tunnel.

The nozzle is 10m in length, and has a throat diameter of 0.084m and an exit diameter of 0.60m. The length of the nozzle expansion section is 7.04m. It is designed to deliver quiet flow at stagnation pressures up to 1 MPa which at the stagnation temperature of 430 K results in a unit Reynolds number of $11 \times 10^6 \mathrm{m}^{-1}$. For these conditions, based on the quiet core length, $Re_L = 40 \times 10^6$.

The expansion section of the nozzle is broken into 20 segments, with the numbering beginning at the nozzle throat. The segment lengths were determined by the maximum tool extension length in the NC-lathe that would maintain the waviness tolerance of 0.023μm that was recommended by Schneider [1998]. The first ten segments of the nozzle expansion (both surrogate and final) have been fabricated by the Notre Dame Hessert Lab Fabrication Shop. The last 10 segments were machined by an outside fabricator.

A unique part of the wind tunnel is a "fast" shutter valve that is located upstream of the

Table 1: Mach 6 Quiet Tunnel Characteristics

Mach number	6.0
Nozzle exit diameter (in)	23.6
Stagnation pressure (quiet flow) (psi)	145
Stagnation temperature (F)	314
Freestream unit Re/ft (quiet flow)	3.34M
Driver tube inside diameter (in)	23.25
Driver tube length (ft)	200
Vacuum tank capacity (k-gal)	66
Run time (ms)	1000
Time between runs (min)	40
Reynolds number variation during run (%)	10
Model length (ft)	3

boundary layer suction slots that are upstream of the nozzle throat. The valve is intended to replace traditional burst plates that in a quiet tunnel, are located at the downstream end of the test section. The use of the fast valve has a number of advantages. The first is that it allows a more rapid turn-around of the tunnel between runs. This changes the measurement approach from placing a large number of sensors on the model to capture a larger spatial sample for a few number of tunnel runs, to using a few or single sensor, that is moved to different spatial locations, particularly off-wall locations that are compiled over a large number of tunnel runs. Another advantage is that by placing the valve upstream of the throat, the test section and and nozzle expansion can be at the vacuum pressure for tunnel start-up. This makes it easier to "start" larger models. Finally the test section never experiences stagnation pressure, which allows the test section structure, and particularly the viewing windows, to be thinner which reduces optical distortion. The reduced loads on the windows allows them to be larger, allowing great visible access.

The overall characteristics of the tunnel are listed in Table 1. The overall cost of the tunnel was $5.4M.

The Mach 6 tunnel was dedicated on November 30, 2018. Figure 1 shows photographs prior to the dedication commencement. The photograph shows the tunnel with the Aluminum surrogate nozzle diverging section. This will be replaced with an identical diverging section of Stainless Steel. The Stainless Steel section is fully fabricated and undergoing polishing.

The tunnel has been undergoing testing. This has involved repeated cycles of the fast shutter valve and documenting of the tunnel flow conditions. Modifications of the shutter valve were required to eliminate binding caused by internal friction points. The redesign of the friction points has been ongoing since the time of the tunnel dedication. However this still remains to be a problem. Work is continuing on finding a long-term solution. This is being headed up by Co-PI Thomas Juliano.

There have been instances when the fast valve was operating in reasonable fashion, and when some documentation of the tunnel conditions could be performed. An example involved total pressure measurements at the end of the nozzle diverging section at the entrance to the test section. This is shown in the photograph in the left part of Figure 2. The right part of Figure 2 shows time traces of the total pressure measured at the contraction inlet, P_{01}, and at the nozzle exit, P_{02}. Total pressure time series measurements reveal the characteristic "pressure stair steps" that

Figure 1: Photograph of Notre Dame Mach 6 Wind Tunnel during dedication in November 2019.

result in a Ludwieg tube arrangement as the expansion wave from the tunnel start reflects back and forth along the driver tube. The time associated with the constant-pressure step corresponds to the length of the driver tube divided by the speed of sound for conditions in the driver tube. In this example, the initial stagnation pressure was 209 kPa (30.3psi). The length of a constant pressure step was approximately 200ms. Over four pressure drop cycles (800ms), the total pressure decreased by 7.1%,. This translates into a 7.1% decrease in the unit Reynolds number. During this sample run, the total pressure fluctuation level, p_0'/P_0, was 2.2% which would signify that "quiet" flow had not been achieved. To date, the reoccurring issues with the fast valve have prevented further documentation of the tunnel flow quality.

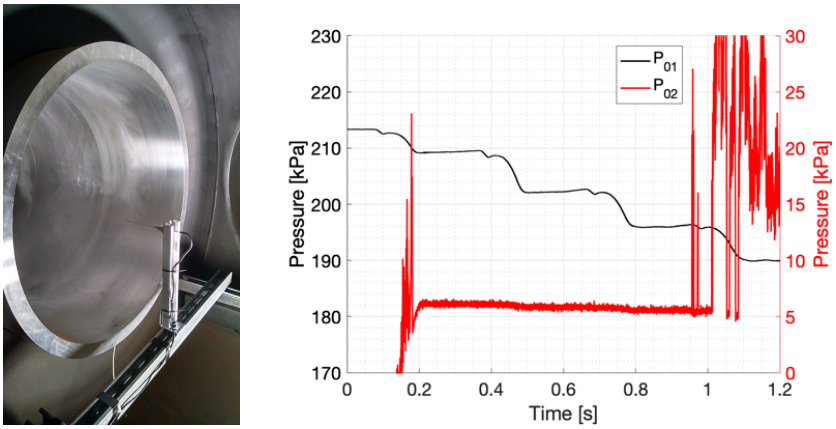

Figure 2: Photograph showing total pressure probe at Mach 6 tunnel nozzle exit used to document flow conditions (left), and sample time traces of total pressure during a run with a 1 atm. differential pressure.

Blunt Cone Frustum Transition. In addition to fabricating the surrogate and primary nozzle expansions, and completing the tunnel with the surrogate nozzle, the program included an experimental component to examine the role of roughness on blunt cone frustum transition. The experiment was originally intended to be performed in the Notre Dame Mach 6 Quiet Tunnel, where it was designed to

1. exploit the large scale of the nozzle and test section while placing the model completely in

the quiet zone, and

2. to utilize nose radii that were large enough to have nose Reynolds numbers that were large enough to result in neutral growth of the 2nd mode instability.

The first criterion was met in the model design shown in Figures 3 and 4. The model is a right-circular cone with a 7° half angle. The length of the cone is 1.6 m (5.27ft) and the base radius is 17.78 cm (7in). The model is designed to have two removable nose tip sections that allow seven different nose tip radii. These are listed as a fraction of the cone base radius in the right part of Figure 3. Figure 4 shows the cone design as it would appear in the Notre Dame Mach 6 Quiet Tunnel test section. The model would fit completely within the nozzle quiet zone.

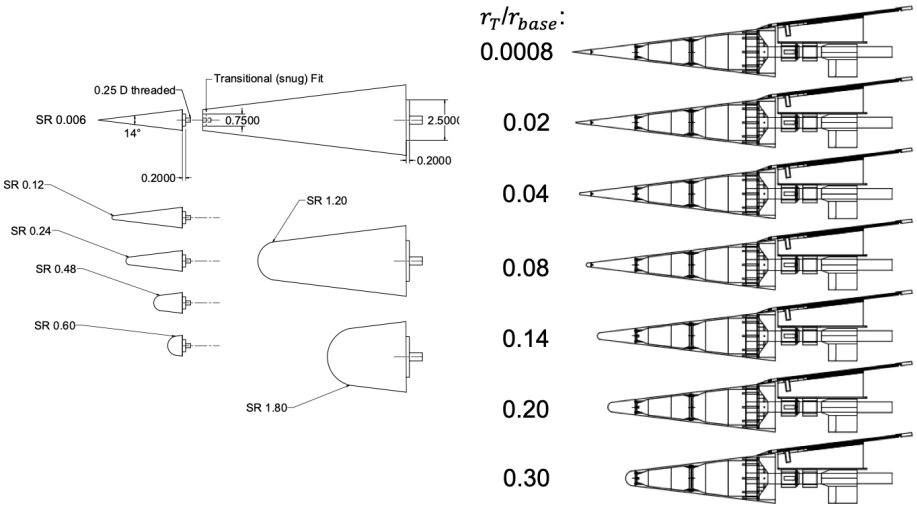

Figure 3: Cone model design with interchangeable nose bluntness tips.

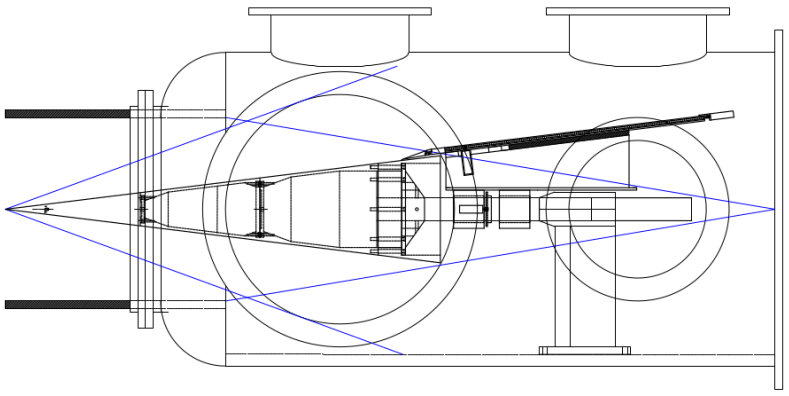

Figure 4: Cone model design shown in Notre Dame Mach 6 Quiet Tunnel.

Figure 5 shows a photograph of the completed cone model along with four of the removable cone tips with radii $r_T/r_{base} = 0.0008$, 0.02, 0.04 and 0.08. The removable nose tips are fabricated in a stainless-steel alloy, and are highly polished. The surface roughness will be quantified using a laser confocal microscope with resolution of 0.5μm.

The model is attached to a 7.6 cm (2.99in) diameter hollow stainless-steel sting that is held in the stainless steel vertical strut. A motorized traversing mechanism mounts on the sting. The traversing mechanism positions a probe in axial, azimuthal and wall-normal directions within the boundary layer. The traversing mechanism has removable wedge tips that can hold a variety of sensors. These are fast-response total pressure and total temperature probes.

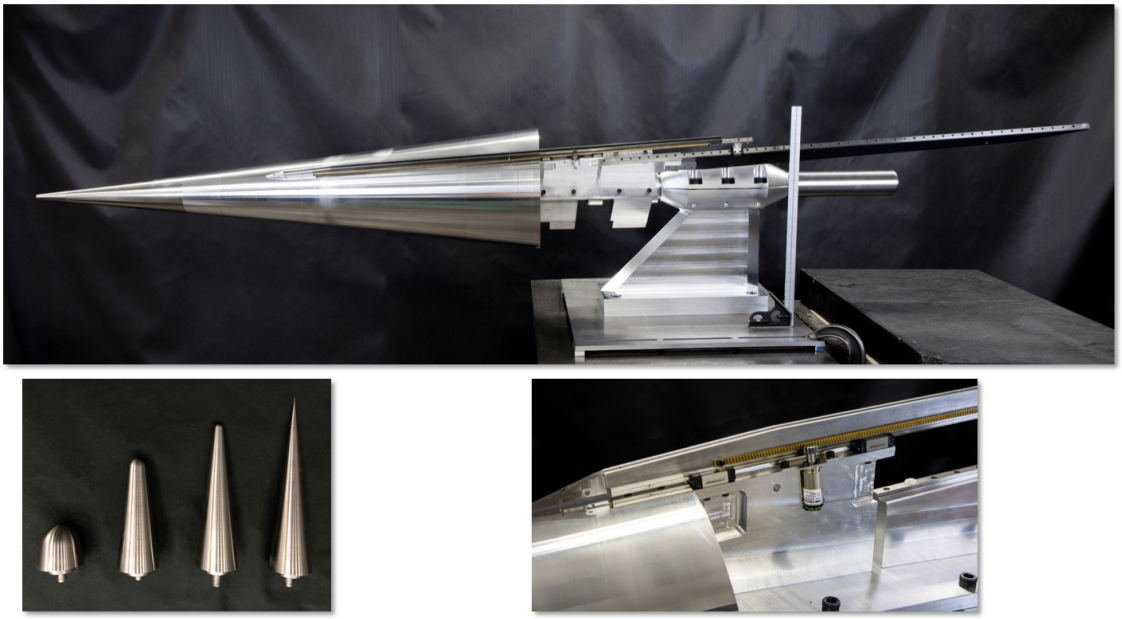

Figure 5: Photograph of blunt cone model mounted on the support sting with 3-D motorized traversing mechanism, and four of the removable cone tips with different nose bluntness.

The experiments were intended to focus on two aspects of blunt cone frustum transition

1. the mechanism for 2^{nd} mode suppression, and
2. the role of nose tip roughness on transition reversal.

The initial focus would involve the four cone tips pictured in Figure 5. At the tunnel maximum quiet design unit Reynolds number of Re = 11M/m (3.34M/ft), these four cone tips have nose Reynolds numbers of $Re_{R_n} \times 10^4 = 0.164$, 3.34, 6.68 and 13.4. Simulations by Batista and Kuehl [2019] indicate that at this unit Reynolds number, the $8\% r_T/r_{base}$ nose tip would result in 2^{nd} mode neutral growth. This is illustrated in Figure 6 which shows N-factor development as a function of frequency, and wall normal profiles of air density, $\sqrt{\rho}$, for $r_T/r_{base} = 0.02$ and 0.08. The premise of Batista and Kuehl [2019] is that 2^{nd} mode suppression is tied to a weakening of the basic flow density gradient. This is evident by the contrast between the wall-normal density profiles for the two nose radii. This is reflected in the 2^{nd} mode N-factors, which for the 8% nose bluntness are $\mathcal{O}30$ times lower than that of the 2% nose bluntness.

The nose radius Reynolds number for the 8% nose bluntness tip under the maximum Reynolds number quiet conditions is represented in Figure 7 which was taken from Paredes et al. [2018]. This shows the length (x) transition Reynolds number as a function of the blunt nose radius Reynolds number for the Stetson [1983] experiments (diamond symbols), and the those of Aleksanfrova et al. [2014] (star symbols). The difference in the Aleksanfrova et al. [2014] experiments, in which

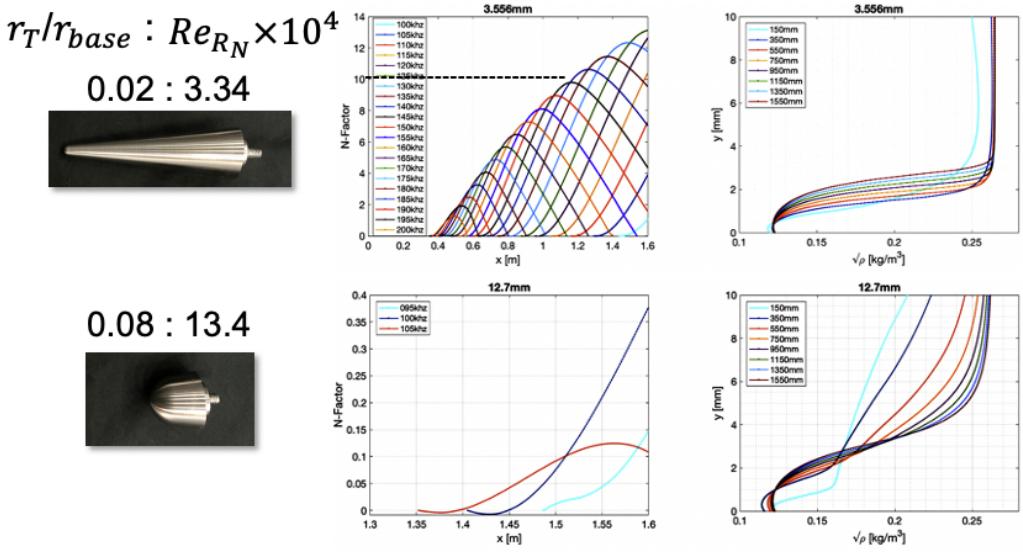

Figure 6: N-factors and wall-normal density profiles for two nose bluntness for maximum quiet design Notre Dame Mach 6 Quiet Tunnel of 11M/m. From Batista and Kuehl [2019].

transition reversal occurs at lower nose radius Reynolds numbers, is presumed to be the result of minute roughness on the blunt nose.

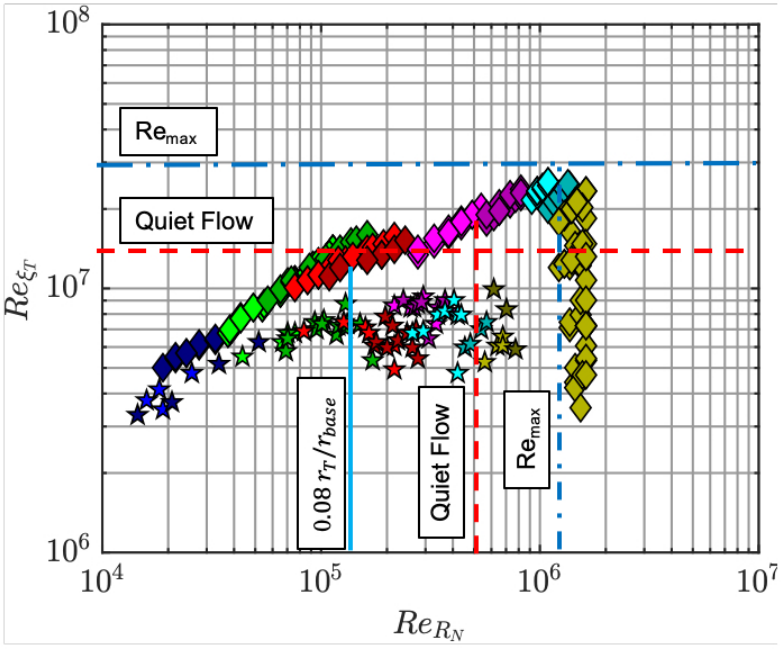

Figure 7: Blunt cone length transition Reynolds number as a function of the blunt nose radius Reynolds number based on Stetson [1983] (diamond symbols), and Aleksanfrova et al. [2014](star symbols). Dashed lines signify quiet and maximum operating conditions of the Notre Dame Mach 6 Quiet Tunnel. Solid vertical line indicates nose radius Reynolds number for 8% bluntness based on maximum Quiet Tunnel conditions.

The horizontal and vertical lines mark the limits of operation of the Notre Dame Mach 6 Quiet Tunnel and the design of the largest 7° half-angle circular cone that will reside completely within the quiet zone. The largest nose radius in this case is 30% of the 17.78 cm cone base radius, or 5.33 cm. The dashed lines correspond to the maximum quiet flow conditions. The solid vertical line corresponds to the nose radius Reynolds number at the maximum quiet unit Reynolds number for the 8% nose bluntness. This clearly intersects with the region of constant transition Reynolds number with increasing nose radius Reynolds number. As with Batista and Kuehl [2019], Paredes et al. [2018] predicts this region corresponds to neutral 2^{nd} mode growth. At this nose radius Reynolds number, the transition Reynolds number is higher for the Stetson [1983] experiment compared to the Aleksanfrova et al. [2014] experiment. The perceived reason is larger nose-tip roughness in the case of the latter.

Experimental and numerical studies[Marineau et al., 2014, Marineau, 2017] indicate that frustum transition in the reversal regime cannot be explained through linear, modal instability theory. Experimental observations such as in Figure 7 indicate that minute surface roughness near the cone tip may offer an explanation. The experimental design is therefore aimed at validating the role of roughness on blunt cone frustum transition. This will initially focus on the 8% nose bluntness tip.

The approach is to apply discrete roughness elements (bumps or dimples) onto the blunt cone tips. The three critical elements of the discrete roughness design are

1. the location of the roughness,
2. the height or depth of the roughness, and
3. the azimuthal wavenumber of the roughness.

Initial guidance on this is based on simulations by Paredes et al. [2017] which are for a hemisphere at Mach 7.32, the results of which are presented in Figure 8. The left plot in Figure 8 shows critical roughness height as a function of the angular location, θ, on the hemispherical tip, where $\theta = 0$ is the stagnation point. The location of the sonic ($M_e = 1$) point is marked by the vertical dashed line at $\theta = 41.1°$. The curves correspond to the critical roughness height based on three different transition correlations relations. Based on these, an average critical roughness height is $k \simeq 0.05$ mm ($\simeq 0.002$ in.).

The right part of Figure 8 is used to address the optimal azimuthal wavenumbers, m and β, of the discrete roughness. The optimal wavenumber depends on the angular location on the hemispherical cone tip, θ_0. The choice of θ_0 is coupled to the critical roughness height as preciously discussed. In some cases there needs to be a compromise between the roughness location and optimal wavenumber based on fabrication limits, i.e., an excessive number of discrete roughness elements.

As an example, two $8\% r_T/r_{base}$ nose tips for the cone design shown in Figure 3 were fabricated. One was made of stainless steel. The other was made of Torlon or Polyamide-Imide (PAI). Photographs of these are shown in Figure 9. As a test, discrete roughness "dimples" were placed on the surface of the Torlon tip at the angular location $\theta = 44°$. The spacing between the roughness corresponded to an azimuthal wavenumber of $m = 400$, which results in an azimuthal angular wavelength of $\lambda_\phi = 0.9°$. The intention was that the dimple diameter to wavelength ratio be $d/\lambda = 0.5$. This ratio is based on discrete roughness criteria for cross-flow transition control[Schuele et al., 2013]. However in this trial, the microscope images indicate that the dimple diameters are smaller than desired. In the use of "dimple" roughness, the assumption is that the depth of the dimple

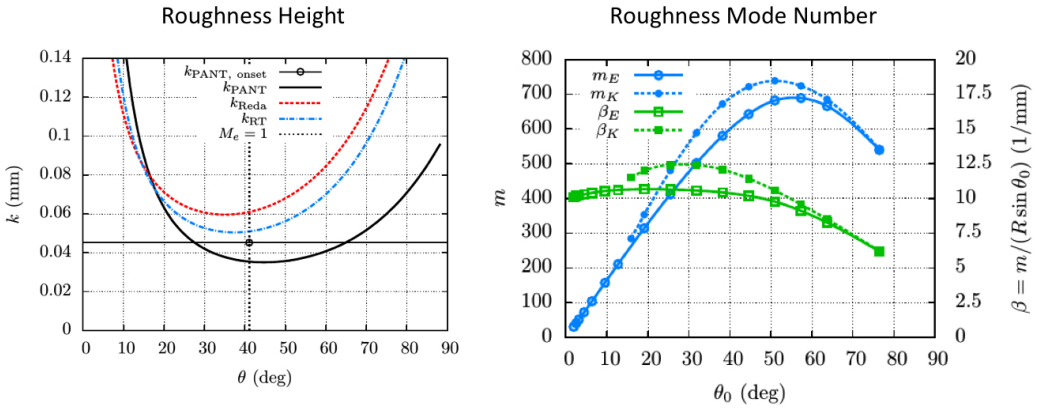

Figure 8: Parameters used in the design of blunt-nose cone roughness. From Paredes et al. [2017]

correlates with the roughness height k. This needs to be proven by experiments that investigate different depths.

More recently we have utilized laser lithography to "drill" small indentations into the surface of cone tips. This is applicable to a number of materials including steel, aluminum, or polymers. Figure]reffig:tip is an example of distributed roughness "dimples" that were laser drilled on the surface of a sharp cone tip made of Torlon. The right side of the figure shows a highly magnified surface profile of the roughness dimples that documents their spatial uniformity. This technique will be applied to the large radii nose tips as well.

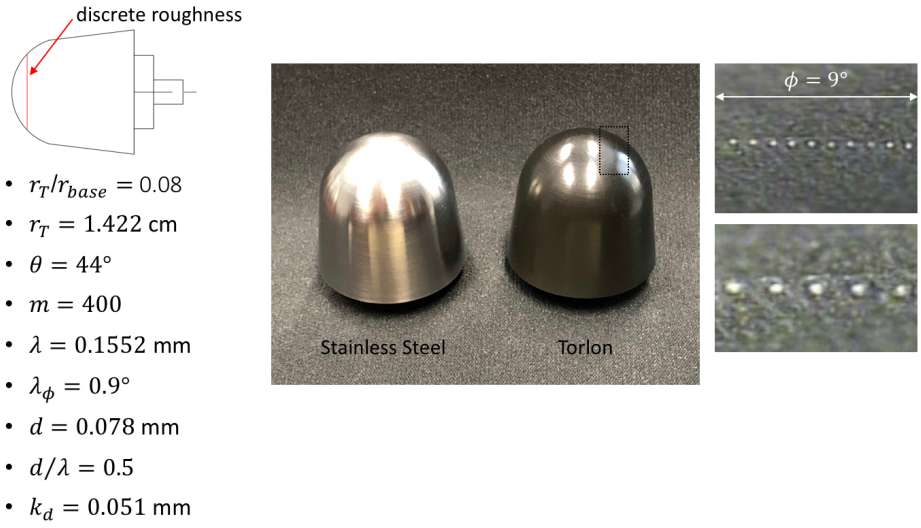

Figure 9: Sample blunt tips of stainless steel and Torlon. The Torlon tip has roughness dimples with $m = 400$ located at $\theta = 44°$.

The simulations by Batista and Kuehl [2019] provide guidance with respect to the maximum 2^{nd} mode frequencies we can expect at transition in the experiments at $Re = 11 \times 10^6 \text{m}^{-1}$. These are summarized in Table for the different cone nose bluntness values. These are based on a N-factor of 10, which has been consistently observed in a number of wind tunnel experiments. Also included

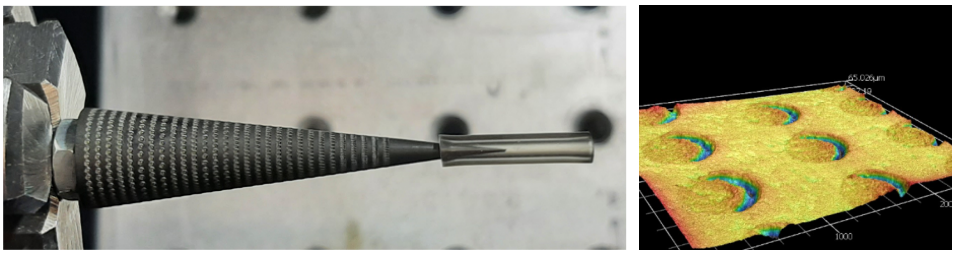

Figure 10: Example of laser-drilled roughness "dimple" cone tips (left) and laser confocal microscope surface profile of roughness showing uniformity of depth and spacing with units of μm.

Table 2: Blunt nose characteristics.

r_T/r_{base} (%)	r_T (mm)	Re_{R_N} ($\times 10^4$)	N	f_{tr}	x_{tr} (m)
0.08	0.150	0.164	10	170	0.8
2	3.048	3.34	10	140	1.3
4	6.096	6.68	10	125	1.5
8	12.192	13.40	-	100	-

in the table are the predicted transition lengths, x_{tr}.

High-bandwidth Total Pressure Probe. In oder to document the 2nd mode development, it was necessary to perform time-resolved total pressure measurements. This involved using a "high-bandwidth" total pressure probe that is mounted on a removable wedge at the leading portion of a traversing mechanism arm. Figure 11 shows a photograph of the total pressure probe wedge mounted on the traversing mechanism. The total pressure probe design consists of a series of concentric hypodermic tubing that is designed with an sensing ID that provides good spatial resolution for wall-normal profiles, along with a tubing length that extends far enough upstream of the support wedge to minimize probe interference. The general requirement is an upstream extension of 10 boundary layer thicknesses. In our case based on Batista and Kuehl [2019], this is approximately 1.2cm. Figure 11 shows the design. The ID and extension length of the Pitot tube design affect the sensor frequency response. Thus the design is a balance between necessary frequency response, and spatial resolution and probe interference. The sensing diameter of the total pressure probe is 0.43mm (0.017in).

The probe uses a Kulite XCS-062, 5psia pressure transducer to convert the total pressure time series to a voltage time series. The pressure transducer is mounted at the end of the 1.2cm long, 0.043mm ID total pressure tubing. It is contained in a 1.59mm ID tubing. The total assembly is contained in the wedge tip on the traversing mechanism. This assembly is aimed at maximizing the frequency response of the measurement system. Dynamic pressure measurements indicated the frequency response of the Kulite/tubing system was from 3-5kHz. Therefore in order to meet the necessary frequency response required to measure 2nd mode waves in the experiment, frequency compensation was needed. This was accomplished through custom-designed analog compensation circuit.

Frequency compensation involved designing a circuit that produce the inverse of the amplitude response of the sensor/system. Typically a tube/pressure sensor represents a 2nd-order system. Thus the compensation circuits should be a series of amplifies with a 2nd-order frequency response.

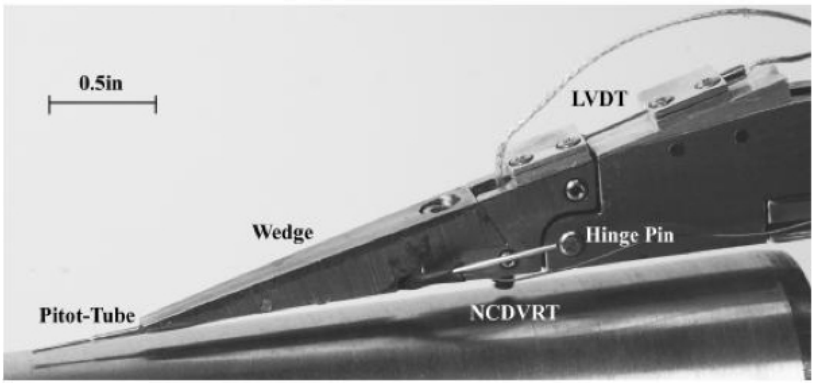

Figure 11: Sensor wedge design for Kulite total pressure probe measurements of frustum transition.

Figure 12 shows the analog frequency compensation circuit designed for this purpose. This is designed to extend the frequency response of the Kulite/tubing system from the original 5kHz to a final cut-off frequency of 200kHz. This more than encompasses the maximum 2nd mode frequency expected in the experiments.

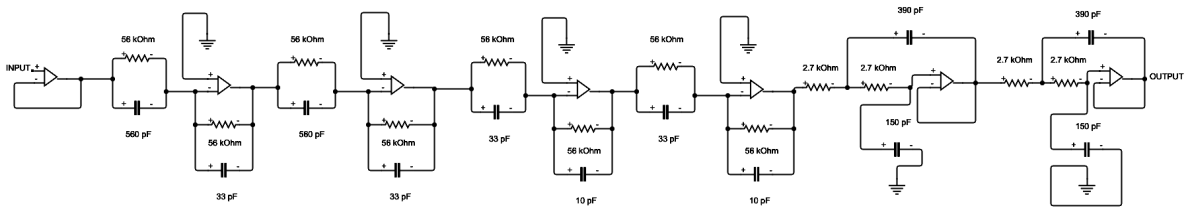

Figure 12: Analog frequency compensation circuit used to extend the frequency response of the total pressure probe system to 200kHz..

The frequency compensation circuit consists of a series of operational amplifier circuits. The first stage is a voltage follower that provides impedance matching. The next four stages is the frequency compensation that extends the bandwidth of the system to 200 kHz. Each is a 2nd-order system that provides 40dB per frequency decade amplification. The cut-in frequencies and damping coefficients of the two 2nd-order stages is tuned to smoothly match the response of the Kulite/tubing 40db/decade decay. The last stage of the circuit is a 2nd-order low-pass anti-alias filter that is needed for the pressure time-series spectral analysis.

The response of the compensation circuit was initially tested by providing a known sinusoidal input and documenting the amplitude response as a function of frequency. The result is shown in Figure 13. This shows the amplitude output (yellow stars) of the compensation circuit as a function of frequency. For reference, 1st-order and 2nd-order responses are also shown The amplitude response of the compensation circuit is observed to provide a 2nd-order response up to the 200kHz cut-off frequency.

The frequency response of the total pressure system was ultimately quantified in a shock tube using a Kulite pressure transducer *without tubing* as a reference. Figure 14 shows a photograph of the shock tube built for this purpose. In the design, a Mylar diaphragm separates air at a given differential pressure produced by pressure and vacuum sources, respectively. The shock tube uses an electric heating wire to activate a run. The signal to the heating wire is also used to trigger

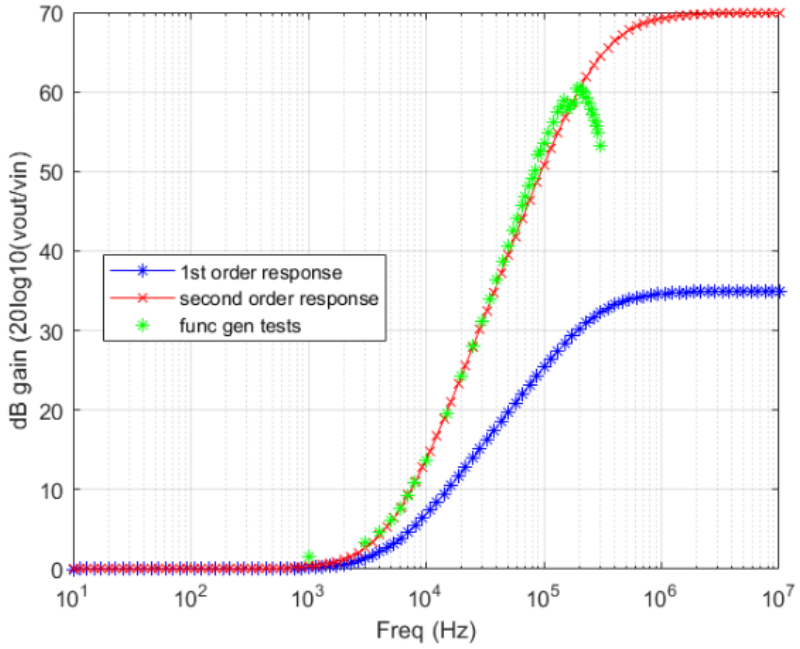

Figure 13: Analog frequency compensation circuit used to extend the frequency response of the total pressure probe system to 200kHz.

data time series acquisition. The test and reference sensors are mounted at the end of the driver tube on the lower pressure side of the diaphragm. The frequency response is determined by the response of the sensor to the pressure rise caused by the shock passage.

An example of the *uncompensated* pressure time series of the Kulite sensor without tubing (reference) and with the probe tubing attached during the passage of a shock wave in the shock tunnel is shown in Figure 15. Considered as a step-input, the rise time provides an estimate of the time response of the system. This illustrates the damping effect that the added pressure tubing has on the response of the total Kulite/tubing system.

A step input associated with the passage of a shock wave is expected to produce a broad band of frequencies. Thus the response of the sensor can be evaluated on the basis of its frequency spectrum. This comparison is presented in Figure 16, which shows spectrum of the response of the reference transducer without tubing, and the spectra of the uncompensated and compensated transducer with tubing. Clearly the compensation circuit extended the frequency response to the designed 200kHz cut-off frequency. The peak in the spectrum at approximately 190kHz is thought to be a resonance in the Kulite transducer circuitry, as it appears in the spectrum of the transducer without tubing.

Fast-response Total Temperature Probe. Simulations by Batista and Kuehl [2019] indicate that with $Re_{unit} = 11$M/m, an 8% nose bluntness would result in neutral growth of the 2^{nd} mode. The premise put forth by Batista and Kuehl [2019] is that 2^{nd} mode growth is tied to a weakening of the basic flow density gradient. This is evident by the contrast between the wall-normal density profiles for the two nose radii that were shown in Figure 6. Therefore one of the objectives of the research is to document the wall-normal density gradient for different nose bluntness and to

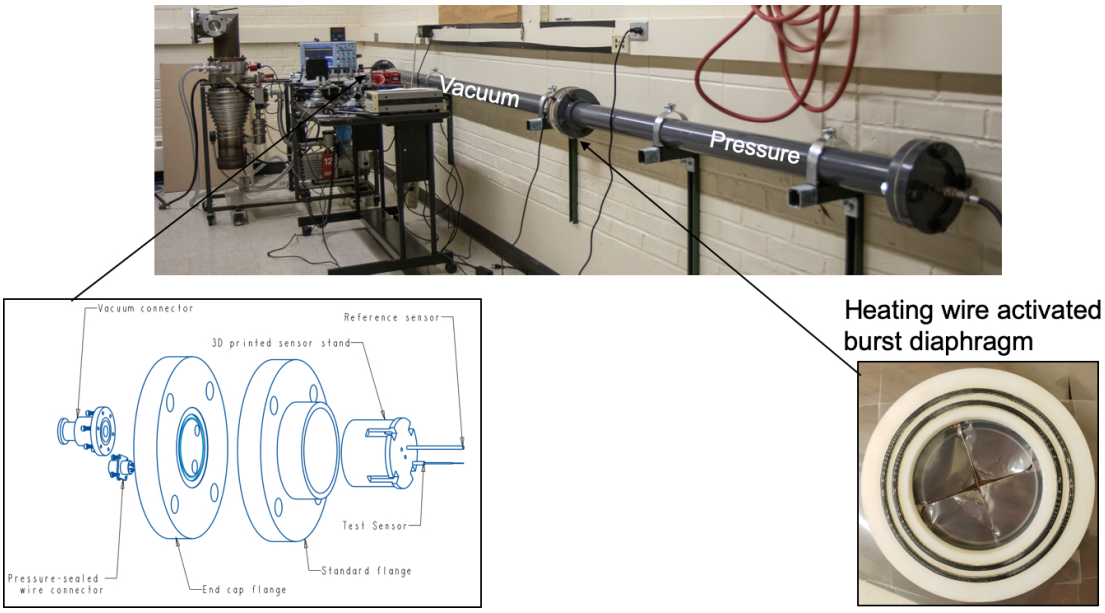

Figure 14: Shock tube developed for dynamic calibration of high-bandwidth total pressure probe for use in the blunt cone frustum transition experiments.

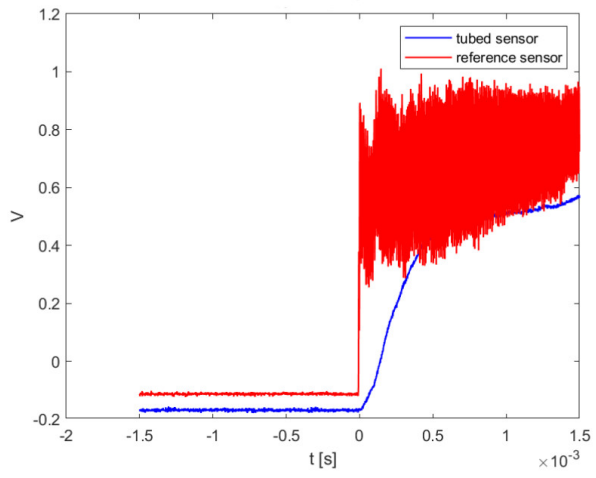

Figure 15: Example of the uncompensated pressure time series of the Kulite sensor without tubing (reference) and with the probe tubing attached during the passage of a shock wave.

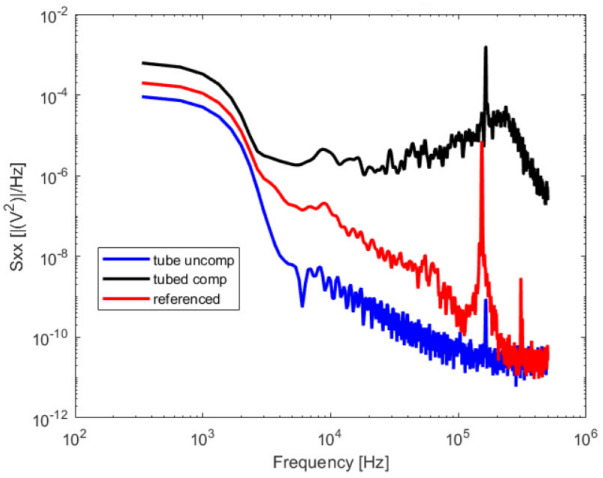

Figure 16: Spectra of the pressure time series obtained during a shock wave passage for the Kulite sensor without tubing (reference), and for the Kulite sensor with probe tubing without and with frequency compensation.

correlate with the nose bluntness, or more specifically with the nose Reynolds number. In order to infer the density gradient, measurements were made of the boundary layer temperature gradient.

For the temperature measurements, we were seeking a robust sensor that was small for good spatial resolution, and had sufficient frequency response for the short run times of a Ludwieg tube. Ultimately we chose to develop a total temperature probe in which the sensing element was a

miniature Type NTC thermistor. Figure 17 shows a schematic view of the total temperature probe. The thermistor fits within the 0.43mm (0.017in) ID tubing used for the total pressure probe, and mounted on the same wedge next to the total pressure probe. The time constant of the thermistor is 20ms.

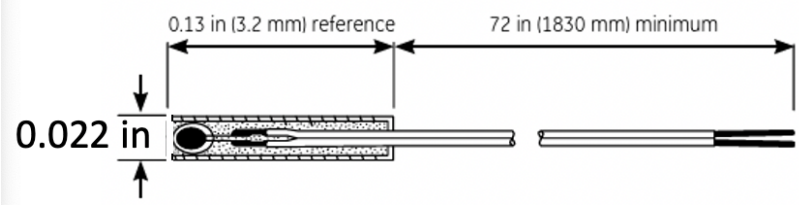

Figure 17: Schematic drawing of total temperature probe based on a miniature Type NTC thermistor.

Thermistors are devices whose electrical resistance is a nonlinear function of temperature. The circuit diagram shown in Figure 18 was used to convert the resistance change into an output voltage change. The output of the circuit as a function of temperature is shown in Figure‘19.

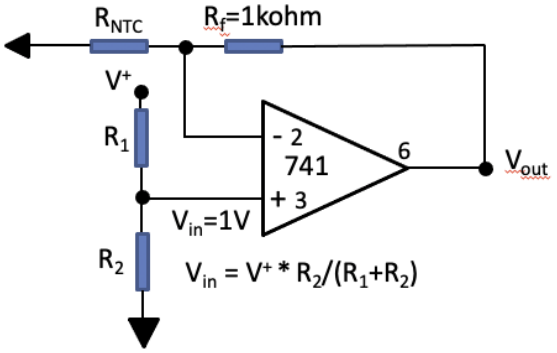

Figure 18: Circuit used to produce voltage output from thermistor sensor.

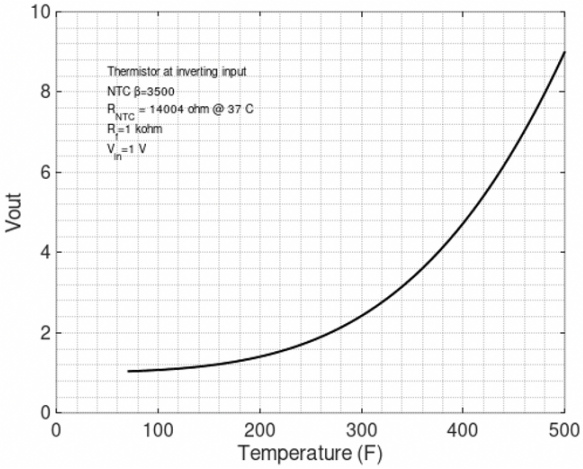

Figure 19: Temperature calibration of thermistor circuit output.

Experiment Setup. As a result of the problems with the fast-valve in the Notre Dame Mach 6 Tunnel, a decision was made in January, 2020 to move the experiment to another Mach 6 wind tunnel, either the 20-Inch Mach 6 Tunnel at NASA Langley Research Center, or in the Mach 6 Ludwieg Tube at the U.S. Air Force Academy. Both of these facilities have similar characteristics including range of unit Reynolds numbers and test section sizes. The NASA tunnel is a blow-down design with a run time on the order of 5 minutes. The Air Force Academy tunnel is a Ludwieg tube design with a short run time of approximately 80ms. However we have used the tunnel in the past as reported by Corke et al. [2018] and Arndt et al. [2020], and therefore we were very familiar with its operation. Both facilities are conventional designs, rather than quiet designs. As preparation for the use of either, we executed a NASA Space Act Agreement with NASA Langley for use of their

Table 3: U.S. Air Force Academy Mach 6 Ludwieg Tube Specifications.

Mach number	5.9±0.6%
Nozzle exit diameter	0.50 m
Test gas	Dry air
T_0	Set to avoid condensation
Re_{unit}	30×10^6 m^{-1}
Nominal run time	∼80ms

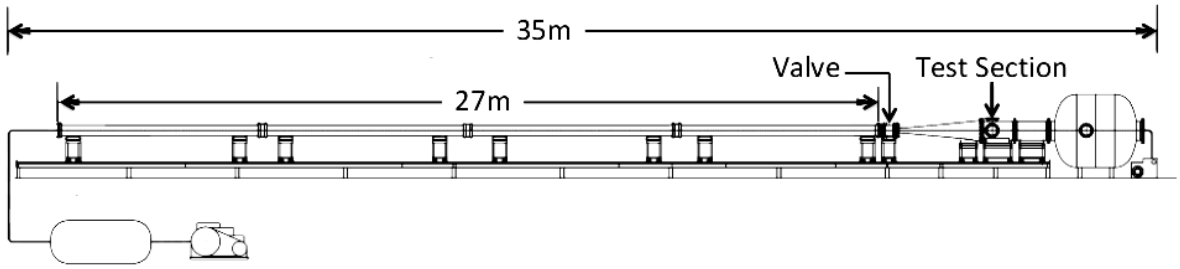

Figure 20: Schematic of U.S. Air Force Academy Mach 6.0 Ludwieg Tube where prior experiments were performed. From Cummings and McLaughlin [2012].

tunnel, and a CRADA agreement with the U.S. Air Force Academy that covered the use of their facility. As a result of the COVID-19 pandemic, the Air Force Academy was the first to become available so that the experiments to date have been conducted there. The characteristics of the U.S. Air Force Mach 6 Ludwieg Tube facility are listed in Table 3.

The facility is based on the design used in the Technical University at Braunschweig, Germany Estorf et al. [2004]. A schematic of the facility is shown in Figure 20. It consists of a 27m long charge tube that is heated and insulated. The pressurized tube discharges through a converging-diverging nozzle from which a Mach 6.0 flow exits into an open-jet test section. A fast-acting plunger valve is located just upstream of the nozzle throat. When the valve opens, an unsteady expansion wave travels both upstream and downstream. The upstream moving expansion wave reflects at the end of the charge tube and then travels downstream until it reaches the nozzle. The time for this sets the duration of quasi-steady flow conditions in the nozzle and the hypersonic test section. At the conditions of the experiment needed to produce a unit Reynolds number of 10×10^6 m^{-1}, the run time was approximately 80 ms. Further details of the facility are given by Cummings and McLaughlin [2012].

The inside diameter of the test section is 0.5 m, and its length is 0.98 m. For optical access, it has three 0.26 m flanged windows, two on opposite sides, and one on top. Measurements in the test section of the sister facility Estorf et al. [2004] confirmed a non-uniformity of the Pitot pressure in the core flow of about ±1.2%, corresponding to Mach number variations of ±0.6%. This non-uniformity results from the narrow wake of the upstream fast-acting valve. To avoid this, the cone model was offset from the centerline of the test section.

The cone model designed for use in the Notre Dame Mach 6 Tunnel is too large for either the NASA or Air Force Academy Mach 6 tunnels. As a result the model used by Corke et al. [2018]

and Arndt et al. [2020] was repurposed. This original model is a thin-walled right-circular cone with a half angle of $\phi_c = 7°$. The original length of the cone is 35.56cm (14in.). The first 4.30cm (1.694in.) of the cone tip is removable. The length of the model was extended by 15.25cm (6in.) by adding an aft aluminum "skirt". The total length of the cone is then 50.8cm (20in.). A schematic drawing and photograph of the modified cone model is shown in Figure 21. Three removable nose tips were fabricated with nose radii, r_n, of 0.15mm, 2.0mm, and 5.33m. The 5.33mm nose radius was the largest that could be placed on the model. The photograph in Figure 21 shows the cone with the 5.33mm nose tip.

The added length of the model was chosen to result in natural 2nd mode turbulent transition to occur at $Re_{unit} = 22$M/m that was possible in both the NASA and Air Force Academy Mach 6 tunnels. This is based in part on simulation results shown in the left part of Figure 22, which shows streamwise N-factor distributions as a function of 2nd mode frequency for the $r_n = 0.15$mm (sharp) nose cone at $Re_{unit} = 22$M/m. The horizontal dashed line marks N=10. We expect transition to occur at the streamwise, x, location where the N-factor curve intersects N=10. This is at approximately $x = 0.4$m, which is 10cm upstream of the end of the cone, which is marked by the arrow on the abscissa.

A second factor in the choice of the $Re_{unit} = 22$M/m is the desire that the largest radius nose tip Reynolds number, Re_{R_N}, be large enough to lead to neutral growth of the 2nd mode. This condition is illustrated in the right part of Figure 22. There the vertical dashed line intersecting the abscissa marks $Re_{R_N} = 11.72 \times 10^4$ based on the $r_n = 5.33$mm cone nose. This is observed to intersect the region where the transition Reynolds number begins to asymptote prior to transition reversal. Simulations[Batista and Kuehl, 2019] indicates the near neutral growth of the 2nd mode accounts for the asymptote in the transition length. This contrast between the sharp (0.15mm) and blunt (5.33mm) nose tips provides the conditions with which to observe changes in the behavior of the 2nd mode growth and decay. The experimental conditions are summarized in Table 4.

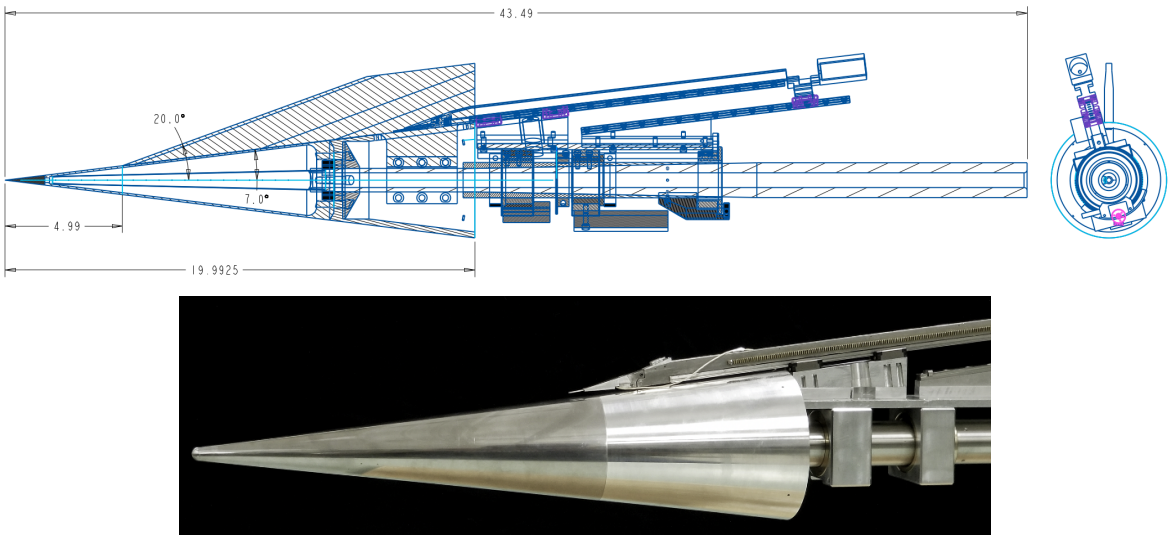

Figure 21: Schematic drawing (top) and photograph (bottom) of the 7° half-angle cone developed for the NASA Langley and U.S. Air Force Academy facilities. These show the cone mounted on the support sting and with 3-D traversing mechanism. Photograph shows model with the 5.3mm radius tip.

The total pressure and total temperature probes were mounted side-by-side in the probe wedge

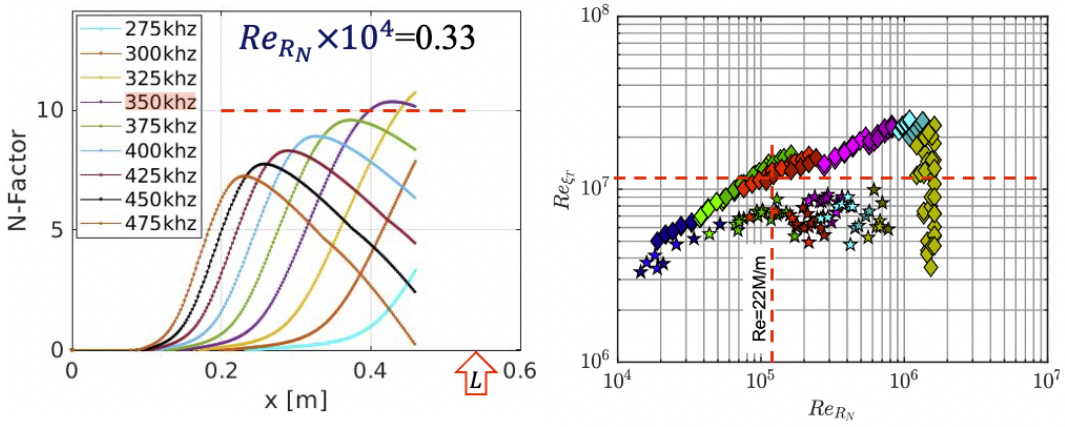

Figure 22: Streamwise N-factor distributions as a function of 2nd mode frequency with $r_n = 0.15$mm (sharp) nose at $Re_{R_N} = 0.33 \times 10^4$, from Batista and Kuehl [2019] (left), and predicted transition Reynolds number for largest model nose radius at $Re_{unit} = 22$M/m, from Paredes et al. [2017].

Table 4: Experimental Conditions.

Re_{unit} (M/m)	r_n (mm)	Re_{R_N} ($\times 10^4$)
11	0.15	0.164
11	2.00	2.200
11	5.33	5.863
22	0.15	0.333
22	2.00	4.840
22	5.33	11.726

that was mounted at the end of the traversing mechanism arm. These could be positioned in in the wall-normal, azimuthal and axial directions in order to document the boundary layer over the cone. All motion was under computer control. The motion resolution in the axial direction was 0.1mm. The resolution in the azimuthal direction is 0.035°, An optical angle encoder provides feedback to the azimuthal positioning. The resolution in the wall-normal direction is 28μm. Figure 23 shows an image of the cone model in the Air Force Academy Mach 6 Ludwieg tube test section.

Preliminary Results. The experimental results presented here are the result of two one-week entries in the Air Force Academy Mach 6 Ludwieg tube. These occurred in January and May of 2021. The January entry was the earliest possible as a result of the COVID-19 pandemic. The following results should be considered to be preliminary. In particular, these were the first trials of the new total temperature probe design, and they indicated the need for some refinement. Another entry to continue the experiments is planned in August, 2021.

The following results correspond to measurements at $x = 42.92$cm (16.9in.) for $Re_{unit} = 11$M/m. Note that $x = 0$ corresponds to the most forward location based on the sharp ($r_n = 0.15$mm) nose tip. Figure 24 shows examples of the total pressure time series at a height above the wall of $y = 0.8$mm for the $r_n = 0.15$mm (sharp) and the $r_n = 5.33$mm (blunt) tipped cone. At this unit Reynolds number, the nose Reynolds number for the sharp and blunt tips are $Re_{R_N} = 0.164$ and 5.863, respectively. Although the nose Reynolds number for the blunt tip is too low to produce

Figure 23: Photograph of cone model in the Air Force Academy Mach 6 Ludwieg tube test section.

neutral growth of the 2nd mode, it is likely large enough compared to that of the sharp tip to provide contrast in the boundary layer development.

A number of markers corresponding to vertical solid and dashed lines of different colors are included on the figures. The solid vertical red line indicates the start of a tunnel run. This is enabled by opening a fast valve located upstream of the nozzle. The dashed vertical red line and the dashed vertical blue mark the beginning and end of the portion of the data time series that is used for statistics. The solid vertical yellow line marks the detected end of a run. In general, the run time corresponding to the time between opening and closing the fast valve was approximately 80ms. In the case of the pressure time series for the blunt tip, shown in the bottom plot in Figure 24, the useable run time was about half that of the sharp tip case shown at the top of the figure.

Figure 25 shows an ensemble of the total pressure time series for the $r_n = 0.15$mm (shown in red) and $r_n = 5.33$mm (shown in blue) at different heights above the wall. These were used to generate the wall-normal distribution of the time-averaged total pressures shown in the left part of Figure 26. These show a contrast between the sharp and blunt tips that we are seeking in order to differentiate the effect of nose bluntness on the 2nd mode instability growth. Both profiles exhibit an inflection that is consistent with documented boundary layer mean velocity profiles for a 7° half-angle cone at Mach 6. An example from Neeb et al. [2018] is given in the right-side plot in Figure 26. In our case, to obtain velocity, the total pressure obtained in the experiment needs to account for the wall-normal variation in the temperature, which of course is one of our objectives given its presumed tie[Batista and Kuehl, 2019] to the 2nd Mode growth rate.

An example of the time series of total temperature obtained in the experiment to date is shown in Figure 27. These are acquired simultaneously with the total pressure time series with the two probes placed next to each other on the probe wedge. These are the companion to the total pressure time series that were presented in Figure 24, and use the same notation to define the useable portion of the time series within a tunnel run. The top plot corresponds to the $r_n = 0.15$mm (sharp) tip, and the bottom plot to the $r_n = 5.33$mm (blunt) tip. There are some obvious differences, although further improvement in the measurement approach is necessary. In particular, the time constant of the sensor is felt to be too large. Although we only seek a time-averaged temperature, the time constant does not allow enough temporal samples to obtain a stable mean value during a 80ms run.

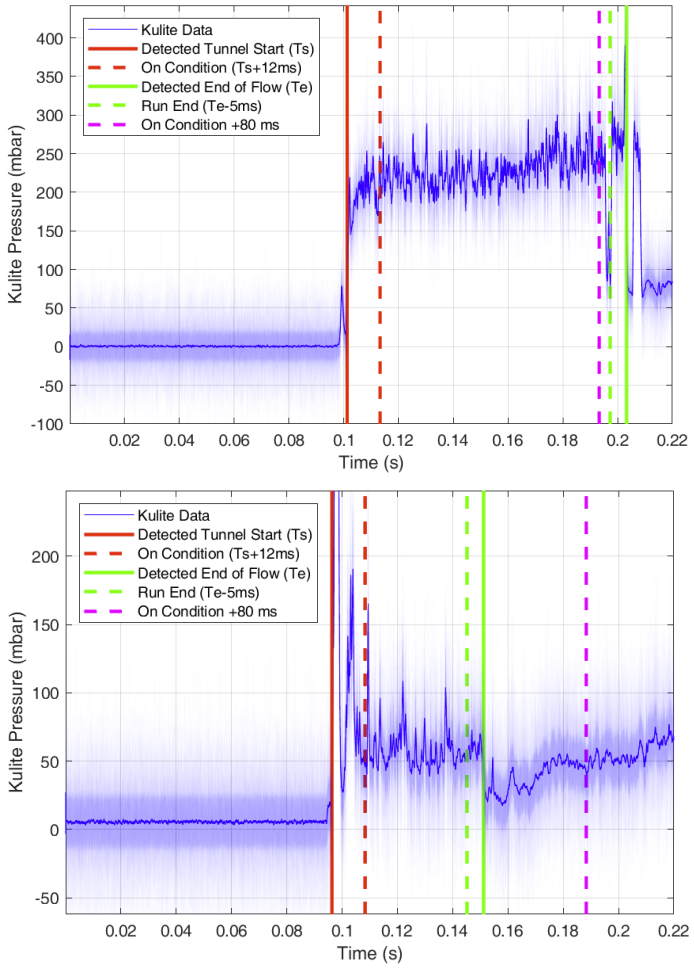

Figure 24: Sample total pressure time series for the $r_n = 0.15$mm (sharp) tip (top) and the $r_n = 5.33$mm (blunt) tip (bottom) at $y = 0.8$mm for $Re_{unit} = 11$M/m .

To correct this, frequency compensation similar to that for the total pressure probe will be applied to the total temperature probe prior to the next planned tunnel entry in August.

Program Summary. The following summarizes the program.

1. The nozzle expansion portion of the Notre Dame Mach 6 Tunnel was fabricated as part of this program. The tunnel was dedicated on November 30, 2018.

2. A large 7° half-angle cone model with removable tips of different nose radii was fabricated for the experimental portion of the program. This included a motorized traversing mechanism that can position probes in the axial, azimuthal and wall-normal directions within the boundary layer. The length of the model makes use of the large test section, and ensures natural turbulent transition will occur on the model under quiet conditions.

3. The Mach 6 tunnel has been undergoing testing. This has involved repeated cycles of the fast shutter valve and documenting of the tunnel flow conditions. Modifications of the shutter

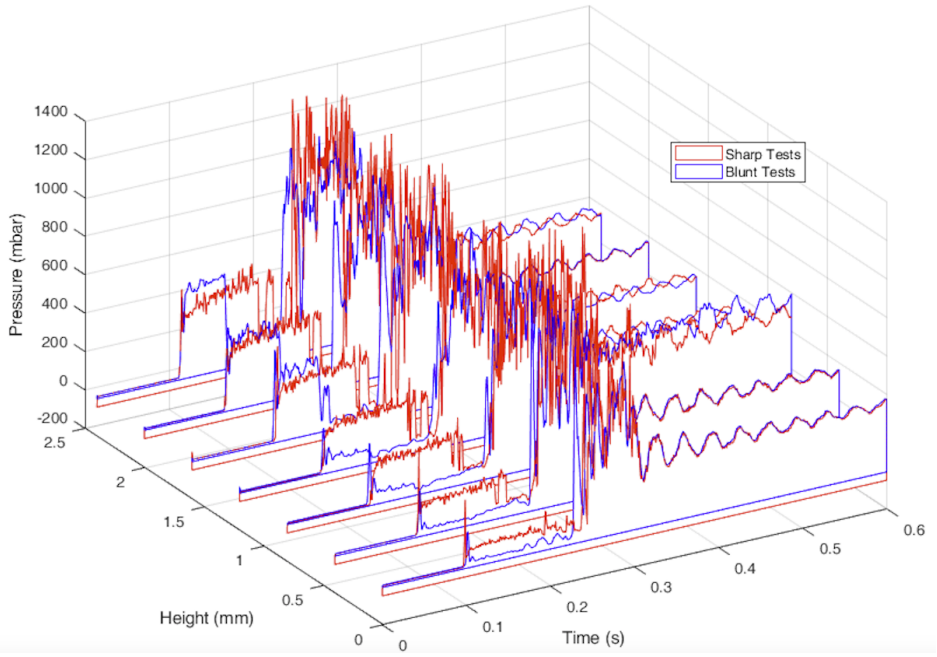

Figure 25: Total pressure time series for the $r_n = 0.15$mm (sharp) tip (red) and the $r_n = 5.33$mm (blunt) tip (blue) at different y distances from the wall for $Re_{unit} = 11$M/m .

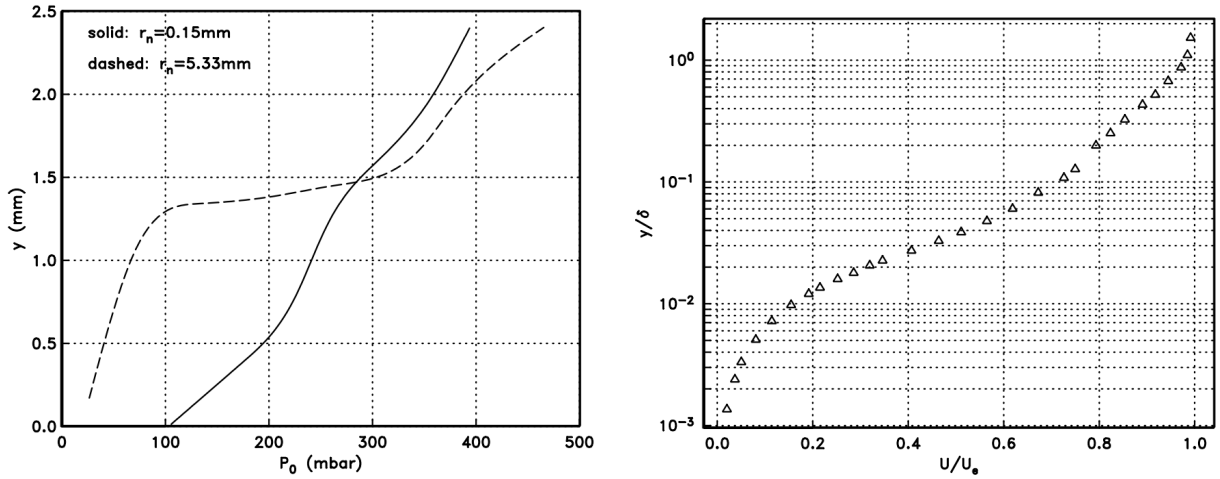

Figure 26: Wall normal profiles of time-averaged total pressure time series for the $r_n = 0.15$mm (sharp) and $r_n = 5.33$mm (blunt) tips for $Re_{unit} = 11$M/m (left) and example of mean profile for sharp-tipped 7° half-angle cone at Mach 6 from Neeb et al. [2018] .

valve were required to eliminate binding caused by internal friction points. The redesign of the friction points has been ongoing since the time of the tunnel dedication. However this still remains to be a problem. Work is continuing on finding a long-term solution. This is being headed up by Co-PI Thomas Juliano.

4. As a result of the problems with the fast-valve in the Notre Dame Mach 6 Tunnel, a decision was made in January, 2020 to move the experiment to another Mach 6 wind tunnel, either

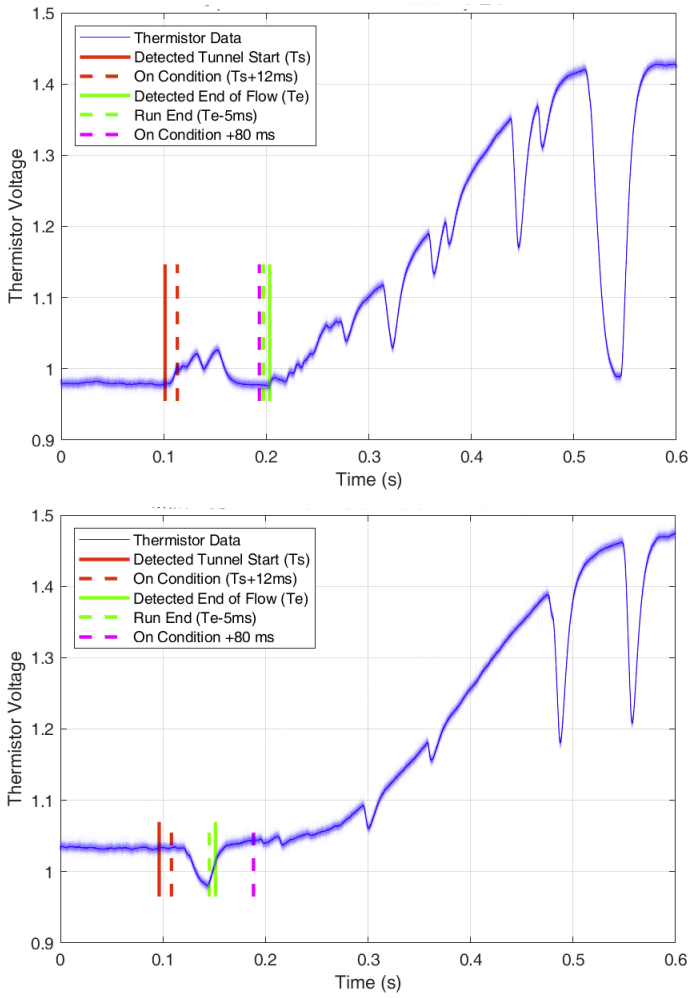

Figure 27: Sample total temperature time series for the $r_n = 0.15$mm (sharp) tip (top) and the $r_n = 5.33$mm (blunt) tip (bottom) at $y = 0.8$mm for $Re_{unit} = 11$M/m .

the 20-Inch Mach 6 Tunnel at NASA Langley Research Center, or in the Mach 6 Ludwieg Tube at the U.S. Air Force Academy. Both of these facilities have similar characteristics including range of unit Reynolds numbers and test section sizes. As a result of the COVID-19 pandemic, the Air Force Academy was the first to become available so that the experiments to date have been conducted there. The objectives of the experiments remained the same as those originally planned for the Notre Dame Tunnel.

5. The cone model designed for use in the Notre Dame Mach 6 Tunnel is too large for either the NASA or Air Force Academy Mach 6 tunnels. As a result, the model used by Corke et al. [2018] and Arndt et al. [2020] was repurposed. This involved increasing the total length of the cone to 50.8cm (20in.) and fabricating three removable nose tips with nose radii, r_n, of 0.15mm, 2.0mm, and 5.33m. The 5.33mm nose radius was the largest that could be placed on the model. The added length of the model was chosen to result in natural 2nd mode transition on the model at an $Re_{unit} = 22$M/m that was possible in both the NASA and Air Force Academy Mach 6 tunnels. A second factor in the choice of the $Re_{unit} = 22$M/m was

the desire that the largest radius nose tip Reynolds number, Re_{R_N}, be sufficient to lead to neutral growth of the 2nd mode.

6. A high bandwidth total pressure probe was developed and documents in a shock tube. This performed well in the Air Force Academy experiments. A fast response total temperature probe was also developed. This utilized a miniature thermistor located within a Pitot probe tube. The two probes were mounted in a measurement wedge that was attached to a motorized traversing mechanism to obtain wall-normal profiles. The total temperature probe design is undergoing some modification that includes frequency compensation needed for the short tunnel runs.

7. Although the experiments were delayed by the COVID-19 pandemic, two one-week wind tunnel entries were performed in January and May of 2021. The processing of those data are still in progress, but preliminary results are promising. Another entry, outside of the official completed program, is planned for August.

Archival publications during this period:

T. Corke and A. Arndt and E. Matlis and M. Semper (2018), Control of Stationary Cross-flow Modes in a Mach 6 Boundary Layer Using Patterned Roughness, J. Fluid Mech., 856, 25 March.

C. L. Running, H. Sakaue, T. J. Juliano (2019), Hypersonic Boundary-Layer Separation Detection with Pressure-Sensitive Paint for a Cone at High Angle of Attack, Exp. in Fluids, 60, 23, pp. 113.

E. Hoberg, C. Huffman, N. Sanchez-Plesha, C. Running, N. Kato and S. Im (2019) , Characteristics of test conditions in the Notre Dame Arc-heated Tunnel, AIAA-2019-3093.

T. Corke and R. Bowersox (2019), Hypersonic Boundary Layer Cross Flow Transition - Characteristics and Control, AIAA J. Spacecraft and Rockets, 36, 2.

T. Corke, E. Matlis, A. Arndt, E. Matlis, R. Bowersox, Ian Neel (2019), Hypersonic Boundary Layer Cross Flow Transition - Characteristics and Control, Chapter 12 of NATO AVT-240 Hypersonic Boundary Layer Transition, NATO S&T Organization, 32 pages.

A. Arndt, T. Corke, E. Matlis, M. Semper (2020), Controlled Stationary/Traveling Cross- flow Mode Interaction in Mach 6 Boundary Layer, AIAA Scitech 2020, Paper 2020-2058, doi.org/10.2514/6.2020-2058.

C. L. Running, T. J. Juliano, M. P. Borg, R. L. Kimmel (2020), Characterization of Post-shock Thermal Striations on a Cone/Flare"" AIAA J., Vol. 58, pp. 2352-2358, May.

H. B. Yates, M. W. Tufts, T. J. Juliano (2020) Analysis of the Hypersonic Cross-flow Instability with Experimental Wavenumber Distributions, J. Fluid Mech., 883, Jan.

C. L. Running, T. J. Juliano, J. S. Jewell, M. P. Borg, R. L. Kimmel (2020), Hypersonic Shock-Wave/Boundary-Layer Interactions on a Cone/Flare, Exp. Thermal and Fluid Science, Vol. 109, Dec.

A. Arndt, T. Corke, E. Matlis and M. Semper (2020) Controlled Stationary/Traveling Cross-flow Mode Interaction in Mach 6 Boundary Layer, J. Fluid Mech., 887, 25 March.

Changes in research objectives: None

Change in AFOSR program manager: Yes

Extensions granted: Yes

Discoveries, inventions, or patent disclosures: None.

References

E. Aleksanfrova, A. Novikov, S. Utyuzhnikov, and A. Fedorov. Experimental study of the laminar-turbulent transition on a blunt cone. *J. Applied Physics and Technical Physics*, 55(3):375–385, 2014.

A. Arndt, T. Corke, E. Matlis, and M. Semper. Controlled stationary/traveling cross-flow mode interaction in mach 6 boundary layer. *J. Fluid Mech.*, 887r, 2020.

A. Batista and J. Kuehl. Implications of local wall temperature variations on second-mode instability. Paper 2019-3084, AIAA, 2019.

I. E. Beckwith, F.-J. Chen, and M. R. Malik. Design and fabrication requirements for low-noise supersonic/hypersonic wind tunnels. AIAA Paper 1988-0143, January 1988.

T. Corke, A. Arndt, E. Matlis, and M. Semper. Control of stationary cross-flow modes in a mach 6 boundary layer using patterned roughness. *J. Fluid Mech.*, 856(10):822–849, 2018.

R. M. Cummings and T. E. McLaughlin. Hypersonic Ludwieg tube design and future usage at the US Air Force Academy. AIAA Paper 2012-734, January 2012.

M. Estorf, T. Wolf, and R. Radespiel. Experimental and numerical investigations on the operation of the Hypersonic Ludwieg Tube Braunschweig. 5th European Symposium on Aerothermodynamics for Space Vehicles, 2004.

M. T. Lakebrink, K. G. Bowcutt, T. Winfree, and T. J. Juliano. Optimization of a Mach 6 quiet wind tunnel nozzle. AIAA Paper 2016-3659, June 2016.

E. Marineau. Prediction methodology for second-mode-dominated boundary-layer transition in hypersonic wind tunnels. *AIAA Journal*, 55(2):484–499, 2017.

E. C. Marineau, C. G. Moraru, D. R. Lewis, J. D. Norris, J. F. Lafferty, R. M. Wagnild, and J. A. Smith. Mach 10 boundary-layer transition experiments on sharp and blunted cones. AIAA Paper 2014-3108, June 2014.

D. Neeb, D. Saile, and A. Gulhan. Experiments on a smooth wall hypersonic boundary layer at mach 6. *Exp. in Fluids*, 59(68):1–21, 2018.

P. Paredes, M. Choudhari, and F. Li. Blunt-body paradox and transient growth on a hypersonic spherical forebody. *Physical Review Fluids*, 2(053903):1–24, 2017.

P. Paredes, M. Choudhari, F. Li, J. Jewell, R. Kimmel, E. Marineau, and G. Grossir. Nosetip bluntness effects on transition at hypersonic speeds: Experimental and numerical analysis under nato sto avt-240. Paper 2018-0057, AIAA, January 2018.

Steven P. Schneider. Design of a Mach-6 quiet-flow wind-tunnel nozzle using the e**N method for transition estimation. AIAA Paper 1998-0547, January 1998.

C-Y Schuele, T. Corke, and E. Matlis. Control of Stationary Cross-flow Modes in a Mach 3.5 Boundary Layer Using Patterned Passive and Active Roughness. *J. Fluid Mech.*, 718:5–38, 2013.

K. Stetson. Nosetip bluntness effects on cone frustrum boundary layer transition. Paper 1983-1763, AIAA, July 1983.